



A Fast Spatial–Spectral NMF for Hyperspectral Unmixing

Taner Ince, Nicolas Dobigeon

► To cite this version:

Taner Ince, Nicolas Dobigeon. A Fast Spatial–Spectral NMF for Hyperspectral Unmixing. IEEE Geoscience and Remote Sensing Letters, 2023, 20, pp.5505305. 10.1109/lgrs.2023.3282218 . hal-04129143

HAL Id: hal-04129143

<https://hal.science/hal-04129143>

Submitted on 15 Jun 2023

HAL is a multi-disciplinary open access archive for the deposit and dissemination of scientific research documents, whether they are published or not. The documents may come from teaching and research institutions in France or abroad, or from public or private research centers.

L'archive ouverte pluridisciplinaire **HAL**, est destinée au dépôt et à la diffusion de documents scientifiques de niveau recherche, publiés ou non, émanant des établissements d'enseignement et de recherche français ou étrangers, des laboratoires publics ou privés.

A Fast Spatial-Spectral NMF for Hyperspectral Unmixing

Taner Ince, *Member, IEEE*, Nicolas Dobigeon, *Senior Member, IEEE*

Abstract—This letter proposes a fast yet efficient method to solve the hyperspectral unmixing problem in the challenging unsupervised context, i.e., when the endmember spectral signatures are unknown. First, a coarse approximation of the hyperspectral image is computed by spatially averaging neighboring pixels, which significantly reduces the amount of pixels to be handled. This reduced set of hyperspectral pixels is unmixed to derive coarse solutions of the unmixing problem, i.e., coarse estimates of the endmember signatures and the corresponding low-resolution abundance maps. Then, the plain resolution abundance maps are estimated from the corresponding hyperspectral image based on the coarse endmember signatures. A sparsity promoting prior exploiting the low resolution map complements the conventional data fitting term to promote spatial smoothness while mitigating the loss of details in the edge areas. Finally, a least square optimization problem is solved to obtain the actual endmember signatures from the hyperspectral image and the abundance maps of plain resolution estimated in the previous step. Numerical experiments show that the proposed method is fast and performs well compared to state-of-the-art approaches from the literature.

Index Terms—Hyperspectral unmixing, non-negative matrix factorization, edge preserving spatial regularization.

I. INTRODUCTION

IMAGING the Earth surface using a hyperspectral (HS) sensor at many narrow wavelengths is known as HS imaging. It is widely used to detect and identify objects of interest in the imaged scene for specified purposes such as surveillance, precision agriculture and environmental monitoring. Although HS sensors offer a high spectral resolution, identifying the materials in the scene remain challenging. One reason lies in the fact that the spatial resolution of the HS sensors does not permit to discriminate subpixel structures, which limits the analysis of the scene in particular when the several materials are mixed in a unique pixel. Spectral unmixing (SU) aims at remedying this issue by computationally recovering the spectral signatures of the elementary materials (also referred to as endmembers) and their corresponding proportions (or abundances) in each image pixel [1].

Part of this work has been supported by the ANR-3IA Artificial and Natural Intelligence Toulouse Institute (ANITI) under grant agreement ANITI ANR-19-PI3A-0004 and in part by the French National Research Agency Active Molecular Imaging and Unmixing (ANR IMAGIN) Project under Grant ANR-21-CE29-0007.

Taner Ince is with the Department of Electrical and Electronics Engineering, Gaziantep University, 27310 Gaziantep, Turkey (e-mail: tanerince@gantep.edu.tr).

Nicolas Dobigeon is with the University of Toulouse, IRIT/INP-ENSEEIH, 31000 Toulouse, France, and also with the Institut Universitaire de France (IUF), 75005 Paris, France (e-mail: nicolas.dobigeon@enseeiht.fr).

Corresponding author: Taner Ince

The observation models for SU are generally classified as linear or nonlinear, e.g., based on the light scattering in the scene [2]. Although nonlinear mixing models are more realistic than the linear ones, in general the simplicity of the linear mixing model (LMM) makes it easy to be implemented and is known to provide a reasonable first approximation of the composition of the scene. LMM assumes that the observed spectra are linear combinations of the endmember spectral signatures weighted by the corresponding fractions. It does not account for the spectral variability which results from atmospheric effects or multiple scattering. Several algorithms have been developed to identify the endmember spectral signatures and estimate the abundances. Geometrical approaches first identify the endmembers as extremal points in the pixels and the abundances are subsequently estimated using a least-square approach [3]–[5]. If a spectral library is available before the analysis, it is possible to find the active endmembers actually involved in the observed mixtures. This problem is known as sparse unmixing and many efficient methods have been designed [6]–[10]. Since the spectral library is composed of a large number of endmember candidates compared to the active ones, the resulting optimization problem are generally granted with a sparsity-promoting prior.

Another solution to the unmixing task consists in formulating SU as a nonnegative matrix factorization (NMF) problem [11] exploiting the fact that the endmember and abundance matrices are composed of nonnegative entries. However, NMF is known to be a nonconvex optimization problem and the recovered solution may dramatically be impacted by noise [12] or the initialization of the iterative algorithm. Therefore, additional constraints and/or penalizations can be considered, e.g., by promoting the sparsity or the spatial homogeneity of the abundance maps. Sparsity promoting norms include the ℓ_1 - [13] or $\ell_{1/2}$ -norms [14]. Further enhancements relying on a sparsity measure have been conducted using local spatial information. For instance, spatial group sparsity regularized NMF (SGSNMF) [15] enforces sparsity of local regions extracted using superpixel segmentation. In [16], graph-regularized $L_{1/2}$ -NMF (GLNMF) minimizes the spectral correlation between pixels by constructing an adjacency matrix. Furthermore, to tackle the problem of sparse noise, robust instances of NMF also relying on an ℓ_1 -norm term have been proposed, see, e.g., [17], [18]. Besides, total variation (TV) has been extensively advocated as a regularization to preserve edges in the estimated abundance map. TV regularized reweighted sparse NMF (TV-RSNMF) combines TV and ℓ_1 -norm regularizations simultaneously [19]. However, combining several regularizers leads to practical

issues when one should adjust their respective weights in the overall objective function. The corresponding hyperparameters may be difficult to adjust and may dramatically impact the quality of the recovered solution. To overcome this issue, one solution consists in designing dedicated prior able to jointly capture the spatial and spectral properties of the HS image. Spectral-spatial weighted sparse NMF (SSWNMF) combines spatial and spectral constraints by spectrally and spatially weighting the ℓ_1 -norm based sparse regularization [20]. Recently, spectral-spatial joint sparse NMF S^2 -NMF has been proposed to exploit the local and global similarities in the data by using a K-means and a superpixel segmentation [21]. Although exploiting the spectral and spatial properties of HS data into a single regularizer yields encouraging results, the corresponding optimization problems generally become harder to solve, resulting in significant increases of the computational burden.

In this paper, we propose a fast method for unsupervised unmixing. The proposed method consists of three steps. In a first step, the HS image to be unmixed is spatially degraded to produce a spatially correlated coarse approximation of the data with a significantly lower number of pixels. This reduced set of pixels are unmixed following an NMF formulation using multiplicative updates to derive coarse estimations of the endmembers and abundances. The second step capitalized on the estimated coarse abundance maps to design a sparsity-promoting regularization to recover abundance maps at full spatial resolution. In a last step, the final estimate of the endmember spectra are derived from the estimated abundance maps and HS image at full resolution. Experiments conducted on simulated and real data sets illustrate the relevance of the proposed method and demonstrate it performs better than state-of-the-art unmixing procedures from the literature.

The main contributions reported in this paper are:

- A low-cost NMF-based spatial-spectral blind unmixing method is designed. Despite its small computational burden, it competes favorably with respect to state-of-the-art methods from the literature.
- NMF is a nonconvex problem whose attained solution highly depends on the initialization. Therefore, this paper reports a simple yet efficient initialization procedure by exploiting the spectral similarities between the pixels.
- A spatial regularization is designed to ensure spatial smoothness while preserving details in the edge areas.

The sequel of the paper is organized as follows. The proposed method is detailed in Section II. Experimental results and comparisons are reported in Section III. Section IV concludes the paper.

II. PROPOSED METHOD

Let $\mathbf{Y} = [\mathbf{y}_1, \dots, \mathbf{y}_N] \in \mathbb{R}^{L \times N}$ denote the set of L -band spectra associated with N pixels composing an hyperspectral image. Each column of the matrix \mathbf{Y} represents the spectrum of each pixel. according to the LMM, the observation matrix is assumed to be decomposed as $\mathbf{Y} = \mathbf{MA} + \mathbf{E}$ where $\mathbf{M} \in \mathbb{R}^{L \times K}$ and $\mathbf{A} \in \mathbb{R}^{K \times N}$ represent the endmember and abundance matrices, respectively, characterized by K endmembers. The matrix \mathbf{E} accounts for the measurement noise

and any mismatch model. The objective of SU is to recover the endmember and abundance matrices \mathbf{M} and \mathbf{A} from the collected data \mathbf{Y} . The main steps of the proposed spatial-spectral NMF-based approach is detailed in the following paragraphs.

A. Coarse approximation of endmembers and abundances

A coarse counterpart $\bar{\mathbf{Y}} \in \mathbb{R}^{L \times \bar{N}}$ of low spatial resolution of the observed image \mathbf{Y} is produced by applying a spectrally- and spatially-invariant averaging filter of size $d \times d$ pixels on each band of the original image with a subsequent subsampling of factor d , i.e.,

$$\bar{\mathbf{Y}} = \mathbf{YBS}_d \quad (1)$$

where \mathbf{B} stands for the average filtering acting on each band and \mathbf{S}_d is a binary matrix for uniform downsampling of factor d in both directions. The \bar{N} spatially correlated pixels composing this coarse HS image are then jointly unmixed using a vanilla instance of NMF. More precisely, coarse estimations $\bar{\mathbf{M}}$ and $\bar{\mathbf{A}}$ of the endmembers and abundance maps are derived by solving the optimization problem

$$\min_{\bar{\mathbf{M}}, \bar{\mathbf{A}}} \frac{1}{2} \|\bar{\mathbf{Y}} - \bar{\mathbf{M}}\bar{\mathbf{A}}\|_F^2 \quad \text{s.t.} \quad \bar{\mathbf{M}} \geq \mathbf{0}, \quad \bar{\mathbf{A}} \geq \mathbf{0} \quad (2)$$

Several algorithms can be advocated to solve this archetypal NMF problem [22]. In this work, without loss of generality, we adopt multiplicative update rules [23] defined as

$$\bar{\mathbf{M}} \leftarrow \bar{\mathbf{M}} \cdot \frac{\bar{\mathbf{Y}}\bar{\mathbf{A}}^T}{\bar{\mathbf{M}}\bar{\mathbf{A}}\bar{\mathbf{A}}^T} \quad \bar{\mathbf{A}} \leftarrow \bar{\mathbf{A}} \cdot \frac{\bar{\mathbf{M}}^T\bar{\mathbf{Y}}}{\bar{\mathbf{M}}^T\bar{\mathbf{M}}\bar{\mathbf{A}}} \quad (3)$$

It is worth noting that the problem (2) is non-convex, which makes the iterative algorithm defined by (3) very sensitive to the initialization. A dedicated initialization procedure is detailed in the Appendix. Finally the coarse approximation of the abundance map $\check{\mathbf{A}} \in \mathbb{R}^{K \times \bar{N}}$ at full resolution is built from the coarse abundance map $\bar{\mathbf{A}}$ at low resolution as

$$\check{\mathbf{A}} = \bar{\mathbf{A}}\mathbf{S}_d^T\mathbf{B}^T. \quad (4)$$

This coarse approximation is subsequently used to design a dedicated regularization, as detailed in the next step.

B. Estimation of abundances at full resolution

The abundance map at high resolution is computed by solving the following penalized least-square problem

$$\min_{\mathbf{A}} \frac{1}{2} \|\mathbf{Y} - \bar{\mathbf{M}}\mathbf{A}\|_F^2 + \lambda \|\mathbf{W} \odot (\mathbf{A} - \check{\mathbf{A}})\|_1 \quad (5)$$

$$\text{s.t.} \quad \mathbf{A} \geq \mathbf{0} \quad \mathbf{1}_K^T \mathbf{A} = \mathbf{1}_N^T$$

In (5), the regularization term promotes a sparse difference between the abundance map \mathbf{A} and its coarse counterpart $\check{\mathbf{A}}$. The spatial weight factor \mathbf{W} is calculated using the coarse abundance map assumed to captures the interpixel spatial structure

$$w_{i,j} = \frac{1}{|\check{a}_{i,j}| + \epsilon}$$

where ϵ a small constant introduced to numerical instabilities. This strategy allows not only to promote spatial smoothness in homogeneous regions but also to preserve the details and

crisp structures in the final estimated maps [24], contrary to the conventional TV regularization which does not account for edge details.

The resolution of (5) can be efficiently conducted by resorting to an alternate direction method of multiplies (ADMM) after introducing two auxiliary variables, i.e.,

$$\begin{aligned} \min_{\mathbf{A}, \mathbf{V}_1, \mathbf{V}_2} & \frac{1}{2} \|\mathbf{Y} - \bar{\mathbf{M}}\mathbf{A}\|_F^2 + \lambda \|\mathbf{W} \odot \mathbf{V}_1\|_1 + \iota_+(\mathbf{V}_2) \\ \text{s.t.} & \quad \mathbf{V}_1 = \mathbf{A} - \tilde{\mathbf{A}}; \quad \mathbf{V}_2 = \mathbf{A}. \end{aligned} \quad (6)$$

Algorithm 1 Estimation of the full resolution abundance map

Input: \mathbf{Y} , $\bar{\mathbf{M}}$, $\tilde{\mathbf{A}}$, λ , $\mu > 0$, ϵ
Initialization: $k = 0$, $\mathbf{V}_1^{(0)}$, $\mathbf{V}_2^{(0)}$, $\mathbf{D}_1^{(0)}$, $\mathbf{D}_2^{(0)}$
1: $\mathbf{A} = \bar{\mathbf{M}}^T \bar{\mathbf{M}} + 2\mu \mathbf{I}$
2: **while** not converged **do**
3: $\mathbf{A}^{(k+1)} = \mathbf{A}^{-1} (\bar{\mathbf{M}}^T \mathbf{Y} + \mu (\mathbf{V}_1^{(k)} + \mathbf{V}_2^{(k)} + \mathbf{D}_1^{(k)} + \mathbf{D}_2^{(k)}))$
4: $\mathbf{V}_1^{(k+1)} = \text{soft}(\mathbf{A}^{(k+1)} - \tilde{\mathbf{A}} - \mathbf{D}_1^{(k)}, (\lambda/\mu)\mathbf{S})$
5: $\mathbf{V}_2^{(k+1)} = \max(\mathbf{0}, \mathbf{A}^{(k+1)} - \mathbf{D}_2^{(k)})$
6: $\mathbf{D}_1^{(k+1)} = \mathbf{D}_1^{(k)} - (\mathbf{A}^{(k+1)} - \tilde{\mathbf{A}} - \mathbf{V}_1^{(k+1)})$
7: $\mathbf{D}_2^{(k+1)} = \mathbf{D}_2^{(k)} - (\mathbf{A}^{(k+1)} - \mathbf{V}_2^{(k+1)})$
8: $k \leftarrow k + 1$
9: **end while**
Output: $\mathbf{A} = \mathbf{A}^{(k)}$

The main steps of the optimization are summarized in Algo. 1. The operators $\text{abs}(\cdot)$, $\text{soft}(\cdot)$ and $\max(\cdot)$ as well as the inversion \cdot^{-1} should be understood as component-wise. The soft-thresholding operator in line 5 is defined as $\text{soft}(t, \delta) = \text{sign}(t) \max\{|t| - \delta, 0\}$.

C. Estimation of the endmembers

After obtaining the high resolution abundance map \mathbf{A} , the actual endmember matrix \mathbf{M} can be computed by solving the following least-square problem

$$\min_{\mathbf{M}} \frac{1}{2} \|\mathbf{Y} - \mathbf{M}\mathbf{A}\|_F^2 \quad (7)$$

whose solution is explicit and easy to compute.

III. EXPERIMENTAL RESULTS

This section report several experiments to assess the effectiveness of the proposed fast NMF-based unmixing method, hereafter coined as FNMF. In particular, it is compared to *state-of-the-art* unmixing methods, namely SSWNMF [20], SGSNMF [15], TV-RSNMF [19], RNMF [17], GLNMF [16], WRNMF [12] and VCA-FCLS [5]. All methods are initialized using VCA [5], as preconized in the corresponding papers. The initializations of the methods under compar The performance of the compared algorithms is evaluated using the average spectral angle distance (aSAD) between the actual \mathbf{m}_k and estimated endmembers $\hat{\mathbf{m}}_k$

$$\text{aSAD} = \frac{1}{K} \sum_{k=1}^K \arccos \left(\frac{\langle \mathbf{m}_k, \hat{\mathbf{m}}_k \rangle}{\|\mathbf{m}_k\| \|\hat{\mathbf{m}}_k\|} \right) \quad (8)$$

while the accuracy of the estimated abundances is measured using the average mean-square error (aMSE)

$$\text{aMSE} = \frac{1}{N} \sum_{n=1}^N \|\mathbf{a}_n - \hat{\mathbf{a}}_n\|^2 \quad (9)$$

TABLE I
SD1: ASAD AND AMSE AVERAGED OVER 10 MONTE CARLO RUNS.

	SNR	FNMF	SSWNMF	SGSNMF	TV-RSNMF	RNMF	GLNMF	WRNMF	VCA-FCLS
aSAD	20	0.0072	0.0240	0.0080	0.0228	0.0223	0.0210	0.0215	0.0330
	30	0.0032	0.0090	0.0047	0.01103	0.0077	0.0084	0.0075	0.0086
	40	0.0015	0.0031	0.0059	0.0034	0.0025	0.0034	0.0039	0.0025
aMSE	20	0.0081	0.0771	0.0160	0.0680	0.0734	0.0676	0.0586	0.0961
	30	0.0045	0.0109	0.0046	0.0088	0.0096	0.0089	0.0098	0.0129
	40	0.0026	0.0026	0.0033	0.0024	0.0024	0.0022	0.0023	0.0026

TABLE II
SD2: ASAD AND AMSE AVERAGED OVER 10 MONTE CARLO RUNS.

	SNR	FNMF	SSWNMF	SGSNMF	TV-RSNMF	RNMF	GLNMF	WRNMF	VCA-FCLS
aSAD	20	0.0105	0.0244	0.0111	0.0242	0.0251	0.0234	0.0236	0.0345
	30	0.0068	0.0095	0.0069	0.0102	0.0095	0.0100	0.0079	0.0122
	40	0.0045	0.0059	0.0078	0.0061	0.0058	0.0064	0.0053	0.0076
aMSE	20	0.0144	0.0540	0.0183	0.0544	0.0601	0.0561	0.0465	0.0636
	30	0.0038	0.0053	0.0048	0.0053	0.0059	0.0059	0.0051	0.0077
	40	0.0010	0.0013	0.0045	0.0014	0.0014	0.0014	0.0012	0.0024

The lower values of aSAD and aMSE imply better estimates of endmember matrix and abundance maps, respectively.

A. Simulated data sets

Two simulated data sets denoted SD1 and SD2 have been generated to compare the algorithms. The two HS images SD1 and SD2 are of spatial size 100×100 pixels and have been created according to the LMM by randomly selecting $K = 9$ spectral signatures from the digital spectral library (splib06) [25] with a spectral ranges between 0.4 and $2.5 \mu\text{m}$. The two data sets differ by their spatial content. The HS image SD1 is mostly composed of flat and smooth regions whereas SD2 has mostly crisp regions. The generated images have been corrupted by an additive Gaussian noise with 3 levels of signal-to-noise (SNR) ratios, i.e., $\text{SNR} \in \{20\text{dB}, 30\text{dB}, 40\text{dB}\}$. The regularization parameters involved in the compared algorithms have been adjusted thanks to a grid search to reach the lowest aSAD and aMSE values. The results have been averaged over 10 Monte Carlo runs. Table I and Table II reports the obtained results for SD1 and SD2, respectively. We can observe that FNMF attains the best aSAD and aMSE values in all but one cases.

Furthermore, as an illustrative purpose, Fig. 1 and Fig. 2 depict the estimated abundance map and the estimated corresponding spectra associated with the endmember #1 for SD1 and SD2, respectively. This results show that the abundance maps and endmembers estimated by FNMF are more similar to reference for both data sets.

B. Real data set

Finally, the compared algorithms have been used to unmix the Cuprite dataset¹. The scene of interest is of spatial size 250×191 pixels. The HS image is originally composed 224 bands, and the bands with low SNR, e.g., corresponding to water absorption, have been removed. Since this data set is not accompanied by ground truth for Cuprite, $K = 12$ reference spectral signatures signatures have been manually collected

¹<http://aviris.jpl.nasa.gov/html/aviris.freedata.html>

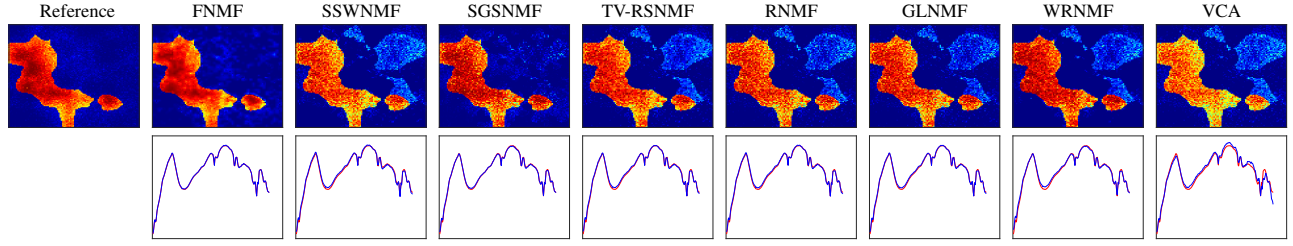


Fig. 1. SD1 (SNR= 20dB): estimated abundance maps (top) and corresponding estimated (blue) and reference (red) spectra for endmember #1 (bottom).

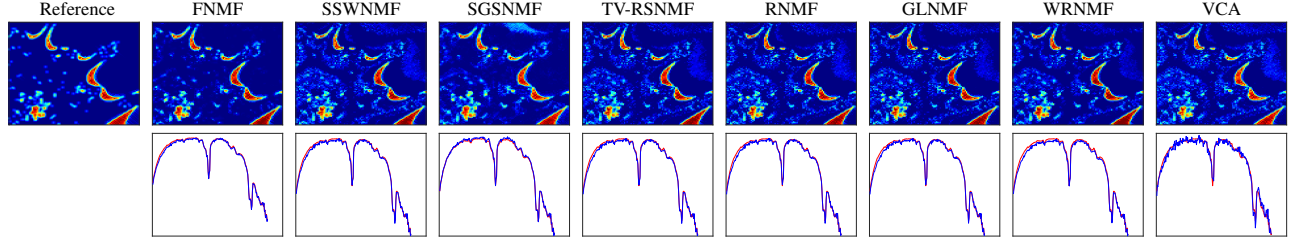


Fig. 2. SD2 (SNR= 20dB): estimated abundance maps (top) and corresponding estimated (blue) and reference (red) spectra for endmember #1 (bottom).

TABLE III
CUPRITE DATASET: aSAD AVERAGED OVER 10 MONTE CARLO RUNS.

Material	FNMF	SSWNMF	SGSNMF	TV-RSNMF	RNMF	GLNMF	WRNMF	VCA-FCLS
Alunite	0.1222	0.0977	0.1514	0.0975	0.0976	0.0976	0.0979	0.0917
Andradite	0.1452	0.1592	0.1342	0.1552	0.1561	0.1559	0.1606	0.1569
Buddingtonite	0.0894	0.0837	0.0944	0.0817	0.0834	0.0833	0.0831	0.0969
Dumortierite	0.0673	0.1343	0.1326	0.1338	0.1341	0.1341	0.1368	0.1200
Kaolinite-1	0.1080	0.1134	0.1107	0.1145	0.1144	0.1143	0.1151	0.1078
Kaolinite-2	0.0916	0.0805	0.0736	0.0811	0.0805	0.0810	0.0843	0.0907
Muscovite	0.0667	0.0824	0.1035	0.0804	0.0812	0.0811	0.0829	0.0788
Montmorillonite	0.0620	0.0598	0.0592	0.0585	0.0590	0.0590	0.0596	0.0692
Nontronite	0.1212	0.1025	0.1032	0.1172	0.1094	0.1096	0.1040	0.1020
Pyrope	0.1001	0.1151	0.1204	0.1151	0.1158	0.1159	0.1156	0.1038
Sphene	0.1074	0.0644	0.0637	0.0666	0.0652	0.0653	0.0656	0.0884
Chalcedony	0.0617	0.1560	0.0676	0.1710	0.1582	0.1585	0.1542	0.1382
Mean SAD	0.0952	0.1041	0.1012	0.1060	0.1046	0.1046	0.1051	0.1037

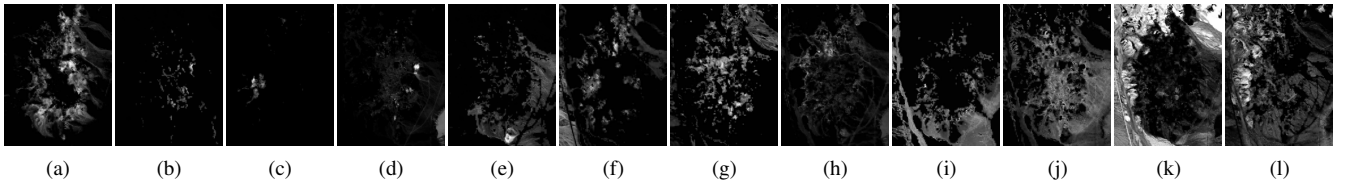


Fig. 3. Abundance maps estimated by FNMF: (a) Alunite. (b) Andradite. (c) Buddingtonite. (d) Dumortierite. (e) Kaolinite-1. (f) Kaolinite-2. (g) Muscovite. (h) Montmorillonite. (i) Nontronite. (j) Pyrope. (k) Sphene. (l) Chalcedony.

in the areas identified in [5]. To identify the materials, the estimated endmembers are compared to spectral signatures in the library splib06. Table III reports the obtained aSAD averaged for 10 Monte Carlo runs. These quantitative results show that that FNMF generally leads to the best results and, in particular, the best mean aSAD. The estimated abundance maps for all minerals are depicted in Fig. 3. Abundance maps recovered by FNMF appear to be spatially consistent.

The computation times required by all algorithms under comparison are reported in Table IV. Interestingly, FNMF is shown to have the lowest computation time, comparable to

VCA-FCLS.

IV. CONCLUSION

This paper proposed a fast unsupervised unmixing method using the spatial and spectral properties of the hyperspectral data. It consisted in a three stage procedure. The first step solved a NMF problem formulated for a coarse counterpart of the image to extract the coarse endmember and abundance maps. In the second stage, the coarse abundance maps were used to design a relevant spatial regularization able to promote spatial smoothness in homogeneous regions but also to

TABLE IV
COMPUTATION TIMES OF THE COMPARED ALGORITHMS (SECONDS).

	FNMF	SSWNMF	SGSNMF	TV-RSNMF	RNMF	GLNMF	WRNMF	VCA-FCLS
SD1	2.2	13.08	16.8	60.5	64.7	15.2	29.07	2.64
SD2	1.9	11.8	79.6	58.7	62.4	17.9	33.79	2.47
Cuprite	16.3	67.2	239.4	256.2	222.2	92	193.11	11.1

preserve the details and crisp structures. In final step, the final endmember estimated were computed. Thanks to extensive experiments conducted on simulated and real data sets, this strategy was shown to yield competitive unmixing results with a significantly lower computational cost when compared to state-of-the-art algorithms.

APPENDIX INITIALIZATION OF THE 1ST STEP

This appendix details the initialization step of the multiplicative updates (3). Spectrally similar pixels in the observed image \mathbf{Y} are identified by conducting an unsupervised clustering using K-means with an Euclidean distance. A coarse counterpart $\tilde{\mathbf{Y}}$ of the data is then computed by averaging the pixels within each cluster, i.e.,

$$\tilde{\mathbf{y}}_n = \frac{1}{|\mathcal{K}_n|} \sum_{k \in \mathcal{K}_n} \mathbf{y}_k \quad (10)$$

where \mathcal{K}_i denotes the set of indices of the pixels belonging to the n th cluster. A geometrical endmember extraction algorithm (e.g., vertex component analysis) [5] is applied to the $\tilde{\mathbf{N}}$ pixels composing $\tilde{\mathbf{Y}}$. The recovered endmember spectra $\tilde{\mathbf{M}}$ are used to initialize the iterative procedure (3). The corresponding initialization of the abundance matrix $\tilde{\mathbf{A}}$ is obtained by solving a fully constrained least square (FCLS) [26] applied to the the spatially coarse HS image $\tilde{\mathbf{Y}}$. Note that this step can be implemented on the principal components of the observed data \mathbf{Y} identified by a subspace identification method, i.e., principal component analysis or HySime [27].

REFERENCES

- [1] N. Keshava and J. F. Mustard, "Spectral unmixing," *IEEE Signal Process. Mag.*, vol. 19, no. 1, pp. 44–57, Jan 2002.
- [2] J. M. Bioucas-Dias, A. Plaza, N. Dobigeon, M. Parente, Q. Du, P. Gader, and J. Chanussot, "Hyperspectral unmixing overview: Geometrical, statistical, and sparse regression-based approaches," *IEEE J. Sel. Topics Appl. Earth Observ. Remote Sens.*, vol. 5, no. 2, pp. 354–379, April 2012.
- [3] M. E. Winter, "N-findr: An algorithm for fast autonomous spectral endmember determination in hyperspectral data," in *Imaging Spectrometry V*, vol. 3753. International Society for Optics and Photonics, 1999, pp. 266–275.
- [4] J. W. Boardman, F. A. Kruse, and R. O. Green, "Mapping target signatures via partial unmixing of AVIRIS data," in *Fifth JPL Airborne Earth Science Workshop*, vol. 95. JPL Publication, 1995, pp. 23–26.
- [5] J. M. P. Nascimento and J. M. B. Dias, "Vertex component analysis: a fast algorithm to unmix hyperspectral data," *IEEE Trans. Geosci. Remote Sens.*, vol. 43, no. 4, pp. 898–910, April 2005.
- [6] J. M. Bioucas-Dias and M. A. T. Figueiredo, "Alternating direction algorithms for constrained sparse regression: Application to hyperspectral unmixing," in *Proc. 2nd Workshop Hyperspectral Image Signal Process., Evol. Remote Sens. (WHISPERS)*, June 2010, pp. 1–4.
- [7] M. D. Iordache, J. M. Bioucas-Dias, and A. Plaza, "Collaborative sparse regression for hyperspectral unmixing," *IEEE Trans. Geosci. Remote Sens.*, vol. 52, no. 1, pp. 341–354, Jan 2014.
- [8] T. Ince, "Superpixel-based graph Laplacian regularization for sparse hyperspectral unmixing," *IEEE Geosci. Remote Sens. Lett.*, pp. 1–5, 2020.
- [9] —, "Double spatial graph Laplacian regularization for sparse unmixing," *IEEE Geosci. Remote Sens. Lett.*, pp. 1–5, 2021.
- [10] N. Dobigeon, J. Y. Tourneret, and C. I. Chang, "Semi-supervised linear spectral unmixing using a hierarchical bayesian model for hyperspectral imagery," *IEEE Trans. Signal Process.*, vol. 56, no. 7, pp. 2684–2695, July 2008.
- [11] D. D. Lee and H. S. Seung, "Learning the parts of objects by non-negative matrix factorization," *Nature*, vol. 401, no. 6755, pp. 788–791, 1999.
- [12] T. Ince and N. Dobigeon, "Weighted residual NMF with spatial regularization for hyperspectral unmixing," *IEEE Geosci. Remote Sens. Lett.*, vol. 19, pp. 1–5, 2022.
- [13] M. D. Iordache, J. M. Bioucas-Dias, and A. Plaza, "Sparse unmixing of hyperspectral data," *IEEE Trans. Geosci. Remote Sens.*, vol. 49, no. 6, pp. 2014–2039, June 2011.
- [14] Y. Qian, S. Jia, J. Zhou, and A. Robles-Kelly, "Hyperspectral unmixing via $l_{1/2}$ sparsity-constrained nonnegative matrix factorization," *IEEE Trans. Geosci. Remote Sens.*, vol. 49, no. 11, pp. 4282–4297, 2011.
- [15] X. Wang, Y. Zhong, L. Zhang, and Y. Xu, "Spatial group sparsity regularized nonnegative matrix factorization for hyperspectral unmixing," *IEEE Trans. Geosci. Remote Sens.*, vol. 55, no. 11, pp. 6287–6304, 2017.
- [16] X. Lu, H. Wu, Y. Yuan, P. Yan, and X. Li, "Manifold regularized sparse nmf for hyperspectral unmixing," *IEEE Trans. Geosci. Remote Sens.*, vol. 51, no. 5, pp. 2815–2826, 2013.
- [17] W. He, H. Zhang, and L. Zhang, "Sparsity-regularized robust non-negative matrix factorization for hyperspectral unmixing," *IEEE J. Sel. Topics Appl. Earth Observ. Remote Sens.*, vol. 9, no. 9, pp. 4267–4279, Sept 2016.
- [18] C. Févotte and N. Dobigeon, "Nonlinear hyperspectral unmixing with robust nonnegative matrix factorization," *IEEE Trans. Image Processing*, vol. 24, no. 12, pp. 4810–4819, Dec. 2015.
- [19] W. He, H. Zhang, and L. Zhang, "Total variation regularized reweighted sparse nonnegative matrix factorization for hyperspectral unmixing," *IEEE Trans. Geosci. Remote Sens.*, vol. 55, no. 7, pp. 3909–3921, 2017.
- [20] S. Zhang, G. Zhang, F. Li, C. Deng, S. Wang, A. Plaza, and J. Li, "Spectral-spatial hyperspectral unmixing using nonnegative matrix factorization," *IEEE Trans. Geosci. Remote Sens.*, pp. 1–13, 2021.
- [21] L. Dong, Y. Yuan, and X. Luxs, "Spectral-spatial joint sparse NMF for hyperspectral unmixing," *IEEE Trans. Geosci. Remote Sens.*, vol. 59, no. 3, pp. 2391–2402, 2021.
- [22] N. Gillis, *Nonnegative Matrix Factorization*. Philadelphia, PA: Society for Industrial and Applied Mathematics, 2020.
- [23] C. Févotte and J. Idier, "Algorithms for nonnegative matrix factorization with the β -divergence," *Neural computation*, vol. 23, no. 9, pp. 2421–2456, 2011.
- [24] T. Ince and N. Dobigeon, "Fast hyperspectral unmixing using a multi-scale sparse regularization," *IEEE Geosci. Remote Sens. Lett.*, vol. 19, pp. 1–5, 2022.
- [25] R. N. Clark *et al.*, *USGS digital spectral library splib06a*. U.S. Geological Survey Denver, CO, 2007.
- [26] D. C. Heinz and C. I. Chang, "Fully constrained least squares linear spectral mixture analysis method for material quantification in hyperspectral imagery," *IEEE Trans. Geosci. Remote Sens.*, vol. 39, no. 3, pp. 529–545, Mar 2001.
- [27] J. M. Bioucas-Dias and J. M. P. Nascimento, "Hyperspectral subspace identification," *IEEE Trans. Geosci. Remote Sens.*, vol. 46, no. 8, pp. 2435–2445, Aug 2008.